

# Simulating and probing many-body quantum states in waveguide-QED systems with giant atoms

C. L. Yang and W. Z. Jia\*

*School of Physical Science and Technology, Southwest Jiaotong University, Chengdu 610031, China*

(Dated: October 29, 2024)

Waveguide quantum electrodynamics (wQED) with giant atoms provides a distinctive opportunity to study one-dimensional (1D) coupled spin systems through its unique decoherence-free interactions. This study presents a theoretical framework for simulating the diagonal Aubry-André-Harper (AAH) model in the context of giant-atom wQED. The proposed scheme employs photonic modes in the waveguide to not only mediate interactions between atoms but also to detect the energy spectrum of the atom array. To illustrate the effectiveness of this approach, we present a simulation of the Hofstadter butterfly spectrum with high precision. Furthermore, for an incommensurate AAH atomic chain, we demonstrate that the photon transmission spectrum can accurately distinguish between the many-body localized phase and the extended phase. The method presented here is also applicable to the simulation of other types of 1D atomic chains based on giant-atom wQED.

## I. INTRODUCTION

Waveguide quantum electrodynamics (wQED) systems [1–3] with giant atoms [4] have emerged as a novel paradigm in quantum optics. In these systems, quantum systems are coupled to distant positions of the waveguide, which are separated by wavelength spacings. The structures of giant atoms have been realized in a variety of quantum systems, including superconducting qubits [5, 6] and giant spin ensembles [7]. Moreover, theoretical proposals have been put forth suggesting the use of cold atoms in optical lattices [8] and synthetic dimensions [9, 10] as a means of realizing the giant-atom configurations. It is evident that giant atoms cannot be regarded as pointlike particles, and thus the conventional dipole approximation is no longer applicable. The non-dipole effects of giant atom systems can produce a number of novel phenomena, including frequency-dependent decay rate and Lamb shift [11], non-Markovian dynamics [5, 12–18], generation of enhanced entanglement [19, 20], tunable atom-photon bound states [21–26] and scattering states [27–34]. One of the most unique properties of giant-atom wQED is the decoherence-free interaction between a pair of braided giant atoms coupling to a linear waveguide [35, 36], which has been successfully implemented in superconducting circuits [6]. This type of protected exchange interactions between giant atoms can be used to perform coherent quantum operations [37, 38]. Another promising application of such decoherence-free interactions is quantum simulation of coupled spins, such as one-dimensional (1D) tight-binding atomic chain [35] and 1D Su-Schrieffer-Heeger (SSH) atomic chain [32].

Quantum simulation provides a robust tool for investigating many-body phenomena that may present a significant challenge for classical computers [39, 40]. The 1D Aubry-André-Harper (AAH) model [41, 42], as a prominent tool for investigating topological physics and local-

ization transition, has attracted considerable attention from theoretical perspectives [43–52]. To illustrate, the diagonal AAH model can be precisely mapped to the two-dimensional (2D) Hofstadter model [53], demonstrating a 2D quantum Hall effect (QHE) with topologically protected edge states, and the corresponding energy spectrum versus the dimensionless magnetic flux form a famous fractal structure known as the Hofstadter butterfly. In addition, the incommensurate diagonal AAH model describes a 1D tight-binding lattice with quasiperiodic potential, in which the disorder strength can induce a delocalization-localization phase transition [42, 43, 47]. Experimentally, the AAH model was first implemented on quantum simulation platforms based on cold atoms in optical lattices [54–56] and photonic lattice [57, 58]. More recently, with the development of modern nanotechnology, superconducting quantum circuits have proven to be an optimal platform for verifying the underlying physics of the AAH model [59–62].

The inherent compatibility of giant-atom wQED systems and superconducting quantum circuits [5, 6] motivates us to investigate the feasibility of simulating AAH models based on giant-atom wQED. Therefore, in this paper, we construct the diagonal AAH model by employing the decoherence-free interactions that are unique to giant-atom wQED systems. In our proposed scheme, photonic modes in 1D waveguide serve not only to mediate interactions between atoms, but also to facilitate the readout of the spectral structure of atomic chain. By appropriately modulating the coupling configurations of the atomic chain, it is possible to reproduce the energy spectrum of the atomic chains with high precision through the photon scattering process. As an example, we demonstrate the efficacy of this method by simulating the Hofstadter butterfly spectrum at high resolution. Moreover, we find that for an incommensurate AAH atomic chain in the extended phase, the decays of the collective modes into the waveguide are concentrated in a few of them. In contrast, in the localized phase, the decays distribute evenly in each mode. This interesting correspondence making the localization transition

---

\* wenzjia@swjtu.edu.cn

easy to detect through the single-photon scattering spectrum. These results also indicate that wQED with giant atoms is optimal for investigating light-matter interactions between an AAH atomic chain and its surrounding photonic environment. The methodology presented here can be extended to simulating other types of 1D atomic chains.

The remainder of this paper is organized as follows. In Sec. II, we derive the single-photon scattering amplitudes for wQED systems with multiple giant atoms based on the real-space formalism [63, 64]. Additionally, we extract the effective Hamiltonian that describes the interacting atomic chain. In Sec. III, we discuss quantum simulation of AAH model through wQED systems with giant atoms. Specifically, we present a method for constructing an AAH-type atomic chain based on giant-atom wQED structure in Sec. III A. Subsequently, we provide discussions on probing the energy band structure, simulating the Hofstadter butterfly, and probing the localization transition through single-photon scattering spectra in Sec. III B-III D. Additionally, we discuss the influence of spontaneous emission to the non-waveguide degrees of freedom in Sec. III E. Finally, further discussions and conclusions are given in Sec. IV.

## II. THEORETICAL DESCRIPTION OF SINGLE-PHOTON SCATTERING IN WAVEGUIDE QED CONTAINING MULTIPLE GIANT ATOMS

In this section, we provide an overview of the single-photon scattering problem for wQED with multiple giant atoms. From the derivation of the single-photon scattering amplitudes, we can extract the effective Hamiltonian describing the inter-atomic interactions mediated by the waveguide modes. This serves as the foundation for the construction of the target Hamiltonian that needs to be simulated. Additionally, in our proposal, single-photon scattering spectra are also employed as a means to probe the many-body states of atomic chains.

### A. Hamiltonian and equations of motion

Here we focus on the wQED structures comprising  $N$  two-level giant atoms with modulated frequencies  $\omega_i = \omega_a + V_0 \cos(2\pi\beta i + \varphi)$  ( $i = 1, 2, \dots, N$ ).  $V_0$  is the modulation amplitude,  $\beta$  controls the periodicity of the modulation, and  $\varphi$  is the modulation phase. Each atom is coupled to a 1D waveguide through two connection points and each pair of neighboring atoms is in a braided configuration, as shown in Fig. 1(a). The connection points are located at position  $x_{im}$  ( $i = 1, 2, \dots, N$ , and  $m = 1, 2$ ), the corresponding coupling strengths are  $g_{i1} \equiv g_1$  and  $g_{i2} \equiv g_2$ , respectively. The phase delays between the coupling points are set as  $\omega_a(x_{i2} - x_{i1})/v_g = \pi$  and  $\omega_a(x_{i2} - x_{i+1,1})/v_g = \phi$  ( $\phi \leq \pi/2$ ).  $v_g$  is the group veloc-

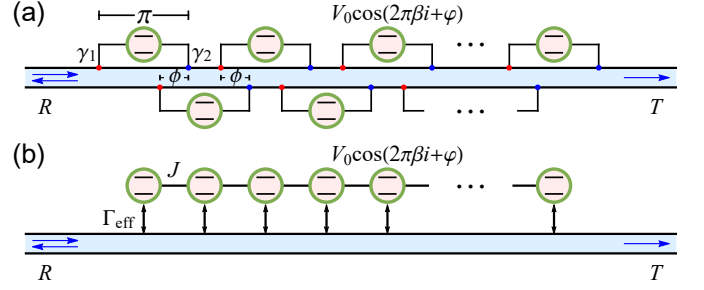


FIG. 1. (a) Sketch of a setup with a braided giant-atom chain realizing an AAH chain with decoherence-free nearest-neighbor couplings. (b) The effective system.

ity of the photons in the waveguide. Under the rotating-wave approximation, the Hamiltonian of the system in the real space can be written as ( $\hbar = 1$ )

$$\begin{aligned} \hat{H} = & \sum_{i=1}^N \omega_i \hat{\sigma}_i^+ \hat{\sigma}_i^- + \int dx \sum_s \hat{c}_s^\dagger(x) \left( -il_s v_g \frac{\partial}{\partial x} \right) \hat{c}_s(x) \\ & + \int dx \sum_s \sum_{i=1}^N \sum_{m=1}^2 g_m \delta(x - x_{im}) [\hat{c}_s^\dagger(x) \hat{\sigma}_i^- + \text{H.c.}], \end{aligned} \quad (1)$$

where  $s = R, L$  and  $l_{R,L} = \pm 1$ .  $\hat{\sigma}_i^+$  ( $\hat{\sigma}_i^-$ ) is the raising (lowering) operator of the atom  $i$ .  $\hat{c}_R^\dagger(x)$  [ $\hat{c}_R(x)$ ] and  $\hat{c}_L^\dagger(x)$  [ $\hat{c}_L(x)$ ] are the field operators of creating (annihilating) the right- and left-propagating photons at position  $x$  in the waveguide.

In the single-excitation subspace, the scattering eigenstate of the system can be written as

$$|\Psi\rangle = \sum_s \int dx \Phi_s(x) \hat{c}_s^\dagger(x) |\emptyset\rangle + \sum_{i=1}^N f_i \hat{\sigma}_i^+ |\emptyset\rangle, \quad (2)$$

where  $|\emptyset\rangle$  is the vacuum state, which means that there are no photons in the waveguide, and meanwhile the atoms are in their ground states.  $\Phi_s(x)$  ( $s = R, L$ ) is the single-photon wave function in the  $s$  mode.  $f_i$  is the excitation amplitude of the atom  $i$ . Substituting Eq. (2) into the eigen equation

$$\hat{H}|\Psi\rangle = \omega|\Psi\rangle \quad (3)$$

yields the following equations of motion:

$$\left( -iv_g \frac{\partial}{\partial x} - \omega \right) \Phi_R(x) + \sum_{i=1}^N \sum_{m=1}^2 g_m \delta(x - x_{im}) f_i = 0, \quad (4a)$$

$$\left( iv_g \frac{\partial}{\partial x} - \omega \right) \Phi_L(x) + \sum_{i=1}^N \sum_{m=1}^2 g_m \delta(x - x_{im}) f_i = 0, \quad (4b)$$

$$(\omega_i - \omega) f_i + \sum_s \sum_{m=1}^2 g_m \Phi_s(x_{im}) = 0. \quad (4c)$$

## B. Scattering amplitudes of photons and effective Hamiltonian of atom array

We assume that a single photon with energy  $\omega = v_g k$  is initially incident from the left, where  $k$  is the wave vector of the photon. Then  $\Phi_R(x)$  and  $\Phi_L(x)$  take the following *ansatz*

$$\Phi_R(x) = e^{ikx} \sum_{p=0}^{2N} t_p \vartheta(x - x_p) \vartheta(x_{p+1} - x), \quad (5a)$$

$$\Phi_L(x) = e^{-ikx} \sum_{p=1}^{2N} r_p \vartheta(x - x_{p-1}) \vartheta(x_p - x). \quad (5b)$$

Here the positions of coupling points from left to right are labeled as  $x_1, x_2, \dots, x_{2N}$ . Moreover,  $x_0 = -\infty$  and  $x_{2N+1} = +\infty$  are defined.  $t_p$  ( $r_p$ ) is the transmission (reflection) amplitude of the  $p$ th coupling point.  $t_{2N} \equiv t$  ( $r_1 \equiv r$ ) is the transmission (reflection) amplitude of the last (first) coupling point.  $t_0 = 1$  is the amplitude of the incident field.  $\vartheta(x)$  denotes the Heaviside step function.

Starting from the equations of motion (4a)-(4c) and the *ansatz* (5a)-(5b), and after some algebra [32], we can obtain the transmission and reflection amplitudes

$$t = 1 - i\mathbf{V}^\dagger (\Delta\mathbf{I} - \mathbf{H})^{-1} \mathbf{V}, \quad (6a)$$

$$r = -i\mathbf{V}^\top (\Delta\mathbf{I} - \mathbf{H})^{-1} \mathbf{V}. \quad (6b)$$

The transmittance and the reflectance can be further defined as  $T = |t|^2$  and  $R = |r|^2$ , respectively. In Eqs. (6a) and (6b),  $\Delta = \omega - \omega_a$  is the photon-atom detuning,  $\mathbf{I}$  is the identity matrix, and  $\mathbf{V}$  takes the form

$$\mathbf{V} = (\mathcal{V}_1, \mathcal{V}_2, \dots, \mathcal{V}_N)^\top, \quad (7)$$

with elements

$$\mathcal{V}_i = \sum_{m=1}^2 \sqrt{\frac{\gamma_m}{2}} e^{i\theta_{im}}. \quad (8)$$

Here the decay rate into the guided modes through the coupling point at  $x_{im}$  is  $\gamma_m = 2g_m^2/v_g$ , and the phase factor is defined as  $\theta_{im} = k_a x_{im} = \omega_a x_{im}/v_g$ . Note that we have assumed that the spacing between the connection points is small enough so that the phase-accumulated effects for detuned photons (the non-Markovian effects) can be neglected. Consequently, the wave vector  $k$  in the definition of the phase factor has been replaced by  $k_a$ .  $\mathbf{H}$  is the effective non-Hermitian Hamilton matrix of the atom array, with elements

$$\mathcal{H}_{ij} = (\omega_i - \omega_a) \delta_{ij} - \frac{i}{2} \sum_{m=1}^2 \sum_{m'=1}^2 \sqrt{\gamma_m \gamma_{m'}} e^{i|\theta_{im} - \theta_{jm'}|}, \quad (9)$$

which summarize the coherent and dissipative atom-atom interactions mediated by the waveguide modes. Moreover, this result indicates that the many-body model of the atomic chain can be designed by optimizing the layout of the connection points and the atom-waveguide coupling rates. Specifically, under parameters  $\theta_{i2} - \theta_{i1} = \pi$  and  $\theta_{i2} - \theta_{i+1,1} = \phi$ , the effective Hamiltonian of the atom array reads

$$\begin{aligned} \hat{H}_{\text{eff}} &= \sum_{i=1}^N \sum_{j=1}^N \mathcal{H}_{ij} \hat{\sigma}_i^+ \hat{\sigma}_j^- \\ &= \sum_i \left[ (\omega_i - \omega_a) - \frac{i}{2} \Gamma_{\text{eff}} \right] \hat{\sigma}_i^+ \hat{\sigma}_i^- \\ &\quad + \sum_{i \neq j} \left( G_{ij} - \frac{i}{2} \Gamma_{ij}^{(\text{coll})} \right) \hat{\sigma}_i^+ \hat{\sigma}_j^-. \end{aligned} \quad (10)$$

Here the effective decay of each atom is defined as

$$\Gamma_{\text{eff}} = 2 \left( \gamma - \sqrt{\gamma^2 - \delta^2} \right), \quad (11)$$

with  $\gamma = (\gamma_1 + \gamma_2)/2$  and  $\delta = (\gamma_2 - \gamma_1)/2$ . And the exchange interaction and the collective decay between the  $i$ th and the  $j$ th ( $i \neq j$ ) atoms take the form

$$G_{ij} = \begin{cases} \gamma \sin \phi \equiv J, & |i - j| = 1 \\ \frac{(-1)^{|i-j|-1}}{2} \Gamma_{\text{eff}} \sin(|i - j| \phi), & |i - j| > 1 \end{cases}, \quad (12a)$$

$$\Gamma_{ij}^{(\text{coll})} = (-1)^{|i-j|-1} \Gamma_{\text{eff}} \cos[(i - j)\phi]. \quad (12b)$$

## III. QUANTUM SIMULATION OF AAH MODEL THROUGH WAVEGUIDE QED SYSTEMS WITH GIANT ATOMS

### A. A scheme for constructing an AAH-type atomic chain using decoherence-free interactions

Now we construct the AAH-type atomic chain based on the decoherence-free interactions between each pair of braided atoms, which is a unique property in giant-atom systems [35]. To this end, we set  $\gamma_1 = \gamma_2 = \gamma$  (i.e.,  $\delta = 0$ , together with  $\theta_{i2} - \theta_{i1} = \pi$ , the condition for decoherence-free interactions between nearest neighbor atoms is satisfied). From Eqs. (11) and (12b), it can be seen that the individual decays and the collective decays all vanish, with  $\Gamma_{\text{eff}} = \Gamma_{ij}^{(\text{coll})} = 0$ . And for exchange interactions, only the nearest-neighbor ones are nonzero, with  $G_{ij} = \gamma \sin \phi \equiv J$  for  $|i - j| = 1$ , and  $G_{ij} = 0$  for  $|i - j| > 1$  [see Eq. (12a)]. Clearly, under these parameters the effective Hamiltonian (10) becomes the standard

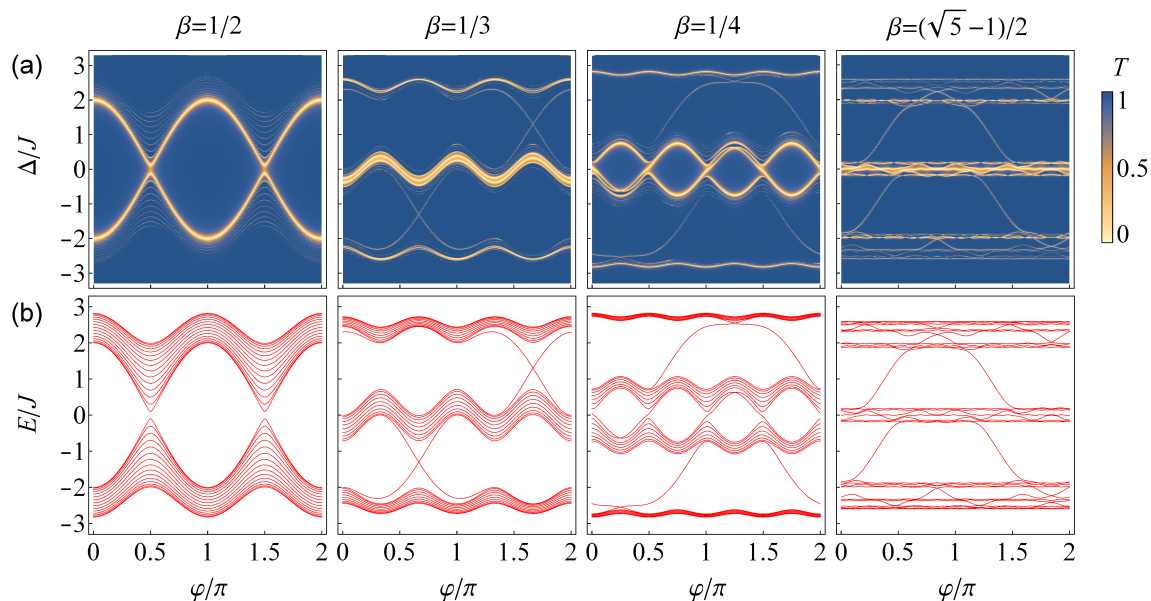


FIG. 2. (a) Transmittance for an AAH giant-atom chain with  $N = 30$  sites as a function of detuning  $\Delta$  and modulation phase  $\varphi$  for different values of  $\beta$ . From left to right,  $\beta$  is chosen as  $1/2$ ,  $1/3$ ,  $1/4$ , and  $(\sqrt{5}-1)/2$ , respectively. The phase delay is selected to be  $\phi = \pi/2$ , resulting in  $J = \gamma$ . Other parameters are set as  $\delta = 0.1\gamma$  and  $V_0 = 2J$ . (b) Energy spectra of an AAH model obtained from theoretical calculations for comparison with (a).

diagonal AAH Hamiltonian

$$\hat{H}_{\text{AAH}} = V_0 \sum_{i=1}^N \cos(2\pi\beta i + \varphi) \hat{\sigma}_i^+ \hat{\sigma}_i^- + J \sum_{i=1}^{N-1} (\hat{\sigma}_i^+ \hat{\sigma}_{i+1}^- + \text{H.c.}). \quad (13)$$

Although a braided atomic chain under the above parameters can be exactly described by a diagonal AAH model, its state cannot be probed by the photon scattering spectra because all the atoms are decoupled from the waveguide. Thus the accuracy of the simulated model must be balanced against the detectability of the atomic chain. This necessitates that the decay rates of the two connection points within each atom should be slightly different, with  $\delta \ll \gamma$ . Under this condition, each atom can obtain a tiny effective decay, which can be approximated as

$$\Gamma_{\text{eff}} \simeq \frac{\delta^2}{\gamma}. \quad (14)$$

Thus the  $i$ th atom can interact with the photonic modes with a strength  $\mathcal{V}_i \sim \sqrt{\Gamma_{\text{eff}}/2}$ . Furthermore, it can be readily demonstrated that for  $\delta \ll \gamma$ , the atom array can still be approximately described by the AAH model. Without loss of generality, we set the phase factor to be  $\phi = \pi/2$ , so the nearest-neighbor interaction strength become  $J = \gamma$ . In addition, for non-nearest-neighbor interactions (with  $|i-j| > 1$ ), we have  $|G_{ij}|/J = \Gamma_{\text{eff}}/(2\gamma) \simeq \delta^2/(2\gamma^2)$  for  $|i-j| \in \mathbb{O}^+$  and

$G_{ij} = 0$  for  $|i-j| \in \mathbb{E}^+$  [see Eqs. (12a)]. For collective decay rates, we have  $\Gamma_{ij}^{(\text{coll})} = 0$  for  $|i-j| \in \mathbb{O}^+$  and  $|\Gamma_{ij}^{(\text{coll})}|/J = \Gamma_{\text{eff}}/\gamma \simeq \delta^2/\gamma^2$  for  $|i-j| \in \mathbb{E}^+$  [see Eqs. (12b)]. These results demonstrate that, in comparison to nearest-neighbor coherent interactions, the non-nearest-neighbor coherent interactions and all dissipative interactions are either negligible or absent. Thus the atomic chain can still be approximately described by the AAH Hamiltonian (13), but each atom weakly couples to the waveguide modes. This implies that the braided atomic chain sketched in Fig. 1(a) is equivalent to the configuration shown in Fig. 1(b). The corresponding scattering amplitudes for incident photons can be calculated by using Eqs. (6a) and (6b).

This approach to achieving many-body quantum simulations has the following features:

(i) The interactions between atoms are mediated by the waveguide modes, which are realized by designing the layout of the connection points. In contrast to conventional methods, direct couplings between atoms are not required.

(ii) In addition to inducing atom-atom interactions, the waveguide also acts as a measurement device, enabling the probing of the energy spectra and quantum states of the atomic chain through the photon scattering process.

(iii) In conventional spectroscopic technique [59, 60] for detecting the spectral structure of a qubit array, it is necessary to perform the measurement on each atom in sequence. This is because measuring a single atom only provides partial information about the energy spectrum. In contrast, our method enables the complete en-

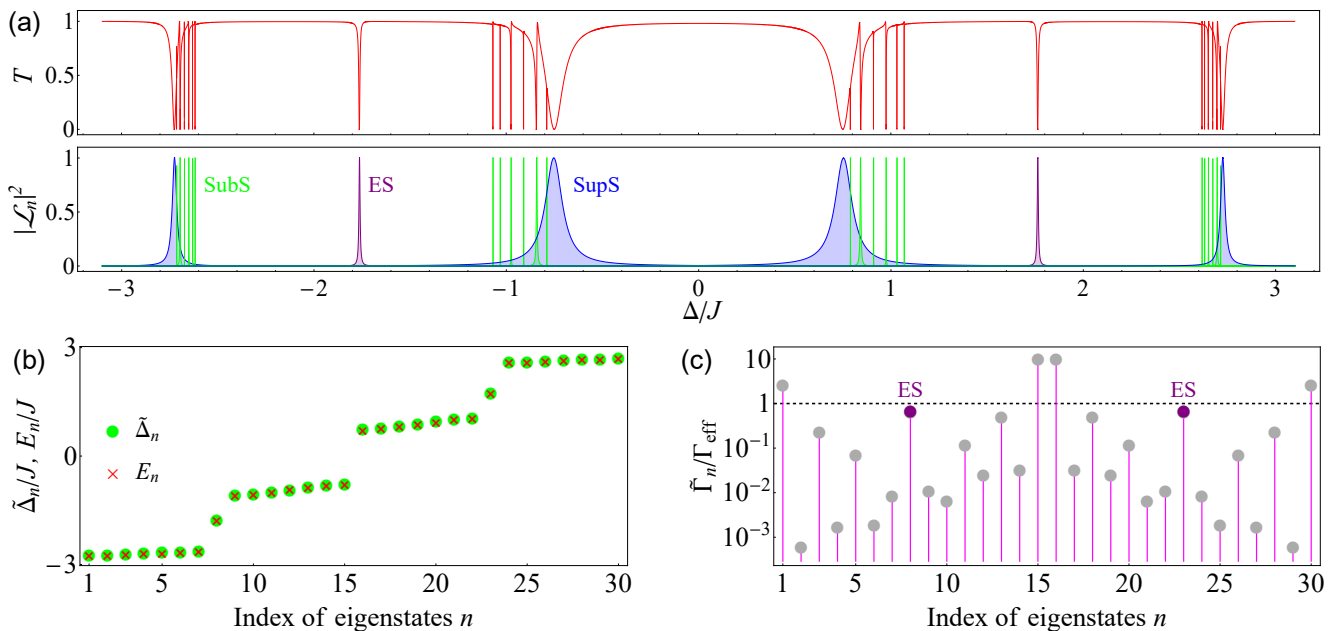


FIG. 3. (a) Upper panel: transmission spectrum for an AAH giant-atom chain, with  $\beta = 1/4$  and  $\varphi = 3\pi/4$ . Other parameters are the same as those used in Fig. 2 (a). Lower panel: the decomposed Lorentzian components for the spectrum shown in the upper panel. The resonances corresponding to the superradiant (subradiant) states in the band are labeled as SupS (SubS), with  $\tilde{\Gamma}_n > \Gamma_{\text{eff}}$  ( $\tilde{\Gamma}_n < \Gamma_{\text{eff}}$ ). The two edge states (ES) in the gaps exhibit a width that is approximately equal to  $\Gamma_{\text{eff}}$ . (b) The center frequency  $\tilde{\Delta}_n$  (the disks) of each Lorentzian component and the eigenenergy  $E_n$  (the crosses) given by the exact AAH model. (c) The linewidth  $\tilde{\Gamma}_n$  of each Lorentzian component. The effective decay  $\Gamma_{\text{eff}}$  of a single giant atom is labeled by the dashed line.

ergy spectrum to be revealed by a single scattering process, as all atoms are coupled to the waveguide. Thus, our proposed measurement scheme may prove to be a highly efficient alternative to existing methodologies.

### B. Probing the energy band structure through single-photon scattering spectra

In Fig. 2(a), we provide the transmittance  $T$  for a lattice with  $N = 30$  as functions of detuning  $\Delta$  and phase factor  $\varphi$  for different values of  $\beta$ . In comparison to the energy spectra obtained through the diagonalization of the AAH Hamiltonian (13) [see Fig. 2(b)], the transmission spectra displayed in Fig. 2(a) can precisely extract the information of the band structures, with the transmission dips corresponding to the eigenenergies of the atomic chain. It is known that the diagonal AAH model can be mapped onto a 2D Hofstadter lattice, where  $\beta$  represents the number of magnetic flux quantum per unit cell and  $\varphi$  denotes the momentum of an additional spatial dimension. In particular, when  $\beta$  is a rational number  $\beta = p/q$  (with  $p$  and  $q$  being coprime), the corresponding energy spectrum is divided into  $q$  energy bands, as shown by the first three panels in Figs. 2(a) and 2(b). And for  $\beta \neq 1/2$ , the energy bands are with nontrivial topology, described by nonzero Chern numbers. Therefore, for a finite-sized system with boundaries considered here, en-

ergy levels corresponding to localized edge modes appear in the gaps. On the other hand, in the case of irrational  $\beta$  [see the last panels in Figs. 2(a) and 2(b)], the spectrum become fractal and form a Cantor set as a result of the quasiperiodicity of the system. The edge states can also be found in the gaps when the system is of finite size.

Moreover, Fig. 2(a) shows that most transmission dips corresponding to the energy levels of the AAH atom array are well resolved. To gain further insight into the formation of this type of spectral structure, we present in the upper panel of Fig. 3(a) the transmission spectrum with  $\beta = 1/4$  and  $\varphi = 3\pi/4$ , and decompose this spectrum into the superpositions of several Lorentzian-type amplitudes contributed by the collective excitations (see Appendix A for details):

$$t = 1 + \sum_{n=1}^N \eta_n \mathcal{L}_n, \quad \mathcal{L}_n = \frac{\tilde{\Gamma}_n}{2 \left( \Delta - \tilde{\Delta}_n + i \frac{\tilde{\Gamma}_n}{2} \right)}. \quad (15)$$

Here  $\tilde{\Delta}_n = \tilde{\omega}_n - \omega_a$  is the detuning between the  $n$ th collective mode and the atomic frequency.  $\tilde{\Gamma}_n$  denotes the effective decay of the  $n$ th collective mode.  $\eta_n$  determines the weight of the  $n$ th Lorentzian component. The obtained Lorentzian components are illustrated in the lower panel of Fig. 3(a).

It can be verified that the center frequencies of the Lorentzian components fit well with the energy levels

given by the exact AAH model [see Fig. 3(b)]. Additionally, as illustrated in Fig. 3(c), only one of the bulk states in each band is superradiant (with  $\tilde{\Gamma}_n > \Gamma_{\text{eff}}$ ), while the remainder are subradiant (with  $\tilde{\Gamma}_n < \Gamma_{\text{eff}}$ ). The superposition and interference between these Lorentzian amplitudes give rise to the transmission spectrum depicted in the upper panel of Fig. 3(a). Finally, the decay rate of the two edge states in the gaps is approximately equal to the effective decay rate  $\Gamma_{\text{eff}}$  of a single atom [see Fig. 3(c)], given that in these states, only the atom at one end is highly excited. It should be noted that the assumptions of  $\delta \ll \gamma$  (resulting in  $\Gamma_{\text{eff}} \simeq \delta^2/\gamma$ ) and  $\phi = \pi/2$  (resulting in  $J = \gamma$ ) have been made to ensure that the atom array can be approximately described by the AAH model. Consequently, the relation  $N\Gamma_{\text{eff}}/J \simeq N\delta^2/\gamma^2 \ll 1$  can be easily satisfied for not so large  $N$ . Namely, the widths of the resonances (the majority of which are smaller than the value of  $\Gamma_{\text{eff}}$ ) are considerably less than the spectrum width (which is of the order of  $J$ ) divided by  $N$ . This property offers a high resolution for the transmission dips associated with the energy levels of the atomic chain, thereby facilitating precise probing of the band structures, as shown in Fig. 3(a). The following section will further illustrate the potential for simulating the Hofstadter butterfly spectrum by exploiting this advantage of giant-atom wQED.

### C. Reconstructing the fractal structure of the Hofstadter butterfly spectrum

It is well known that the problem of Bloch electrons on a 2D lattice subject to a perpendicularly applied magnetic field is described by the Hofstadter model. When the magnetic field reaches a strength that allows one magnetic flux quantum per unit cell to pass through, the corresponding energy spectrum versus the dimensionless magnetic flux form a famous fractal structure known as the Hofstadter butterfly [53]. Nevertheless, a magnetic field of approximately  $10^4\text{T}$  is necessary to observe the Hofstadter butterfly in typical crystals, which is beyond the capabilities of current experimental techniques. One potential solution to this challenge is the use of superlattices with a larger lattice constant, which could reduce the requisite strength of magnetic fields [65–67]. On the other hand, the 2D Hofstadter model can be exactly mapped to the 1D diagonal AAH model. Consequently, the Hofstadter butterfly spectrum has also been successfully simulated in 1D AAH-type chains based on superconducting circuits [59, 60]. In this approach, the modulation frequency  $\beta$  is used to analogize the required magnetic flux, thereby eliminating the need for a complex 2D lattice and an external magnetic field.

As previously outlined in Sec. III A, in our proposal on generating a diagonal AAH model based on giant-atom wQED, the waveguide modes serve two distinct purposes. Firstly, they mediate decoherence-free interactions between neighboring atoms. Secondly, they provide

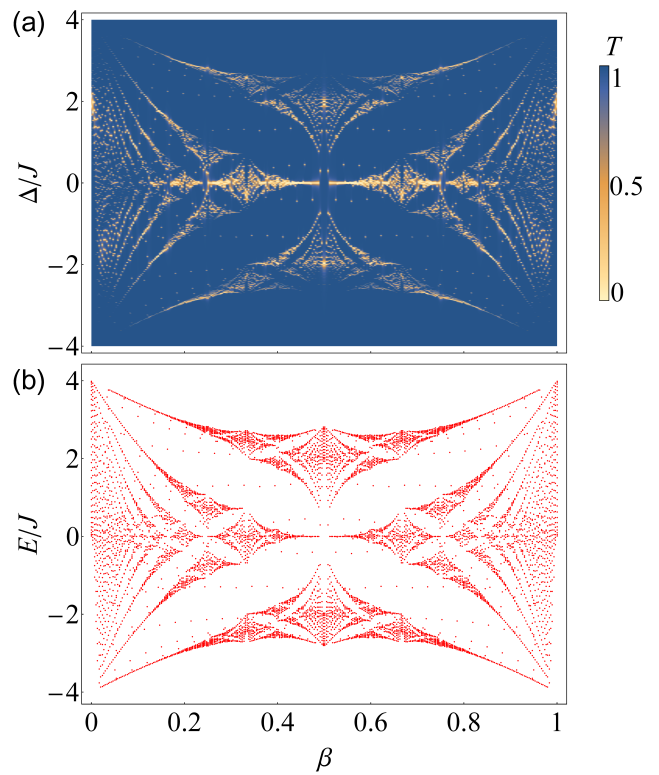


FIG. 4. (a) Quantum simulation of Hofstadter butterfly using scattering spectra of a giant-atom wQED setup. The modulation phase is set as  $\varphi = 0$ . The modulation frequency  $\beta$  is varied from 0 to 1, generating 299 distinct instances of the transmission spectrum. Other parameters are the same as those used in Fig. 2(a). (b) The theoretical Hofstadter butterfly energy spectrum obtained from the AAH Hamiltonian.

channels for probing the energy spectrum of the atom array. Moreover, as demonstrated in Sec. III B, the majority of the resonance dips corresponding to the energy levels of the AAH model can be well resolved in the transmission spectrum. Therefore, the scattering spectrum of this system can be effectively utilized to reconstruct the complex and fine fractal structure of the Hofstadter butterfly spectrum with a high degree of fidelity, as shown in Fig. 4(a). In this panel, the number of giant atoms is set to  $N = 30$ , and the reduced magnetic flux  $\beta$  is varied from 0 to 1. This generates 299 distinct instances of the reflection spectrum, which exhibit clear fractal features and a shape that is reminiscent of a butterfly. Figure 4(b) depicts the Hofstadter butterfly energy spectrum obtained from the theoretical model, which exhibits a high degree of agreement with the result in Fig. 4(a). Thus, it appears that an alternative or potentially more efficient approach to simulating the Hofstadter butterfly spectrum is feasible.

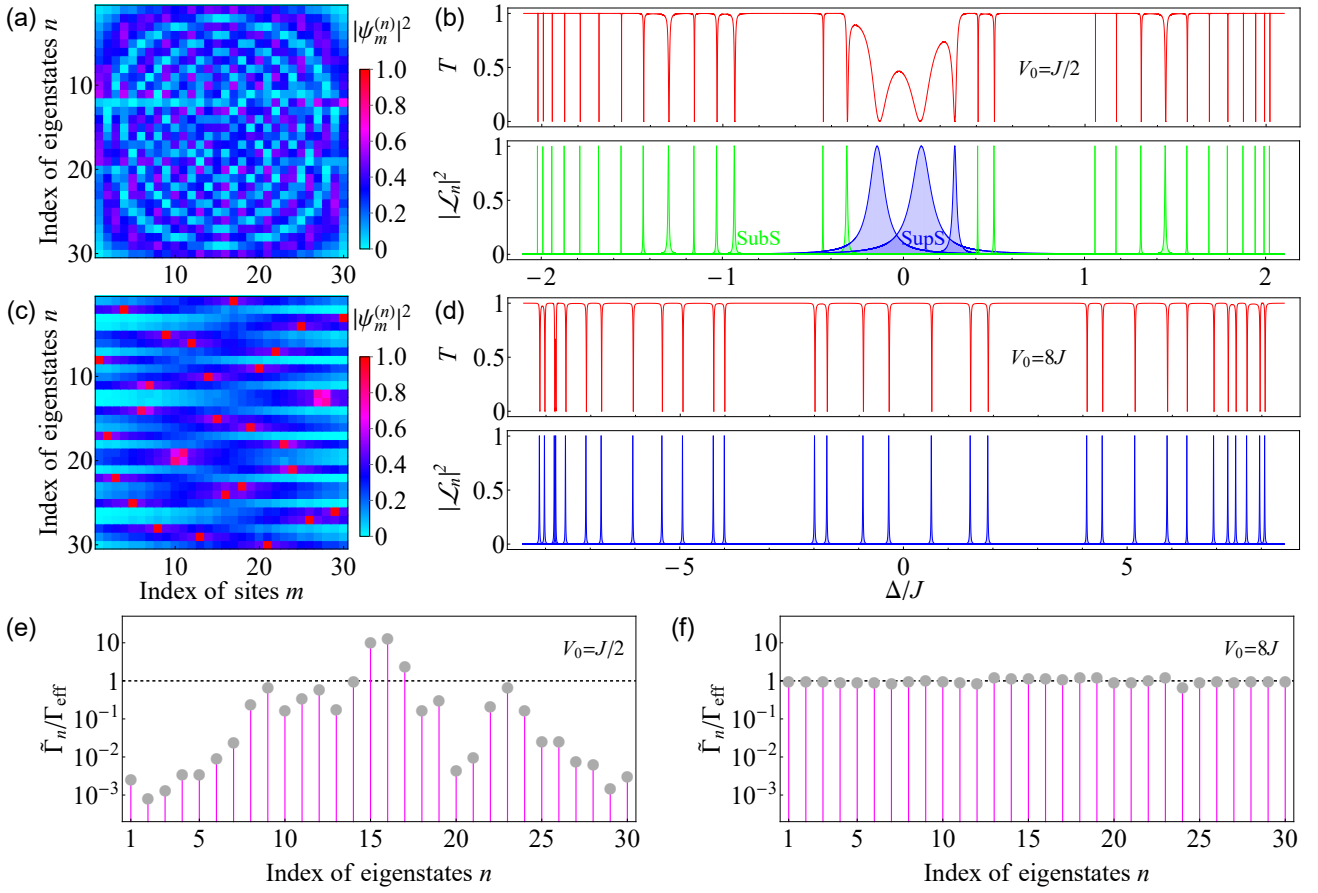


FIG. 5. (a) The square of the modulus of the wave functions of AAH model with  $N = 30$ ,  $V_0 = J/2$ ,  $\beta = (\sqrt{5} - 1)/2$ , and  $\varphi = 0$ . (b) The transmission spectrum (upper panel) and corresponding Lorentzian decompositions (lower panel) for a wQED system with an AAH-type giant-atom array. The phase delay is selected to be  $\phi = \pi/2$ , resulting in  $J = \gamma$ . The quantity  $\delta$  is chosen as  $\delta = 0.1\gamma$ . The size of the array and the on-site modulations are the same as in (a). In the lower panel, the resonances corresponding to the superradiant (subradiant) states are labeled as SupS (SubS). (c) and (d) Similar to (a) and (b), but with  $V_0 = 8J$ . (e) and (f) The decay rate  $\tilde{\Gamma}_n$  of each Lorentzian component for  $V_0 = J/2$  and  $V_0 = 8J$ . The effective decay  $\Gamma_{\text{eff}}$  of a single giant atom is labeled by the dashed line.

#### D. Probing the localization transition

The localization transition [42, 43, 47] is another interesting topic in an incommensurate diagonal AAH model. When the on-site potential of the diagonalized AAH model is made quasiperiodic by setting  $\beta$  to an irrational number, the model exhibits a localization transition, where all bulk eigenstates are extended for  $V_0 < 2J$ , and localized for  $V_0 > 2J$ . Here we will present an intriguing correlation between the localization transition of the atomic chain and the photon transport behavior observed in the waveguide.

To analyze the relation between the localization transition and the scattering spectrum, we let the value of modulation frequency irrational, with  $\beta = (\sqrt{5} - 1)/2$ , and present in Fig. 5(a) the square of the modulus of the wave functions  $\psi_m^{(n)}$  (where  $m$  and  $n$  are used to index the sites and eigenstates, respectively) of the di-

agonal AAH model for  $V_0 = J/2$ , which corresponds to the extended phase. The resulting transmission spectrum and the corresponding Lorentzian decompositions are illustrated in Fig. 5(b). These collective modes with extended feature comprise a small number of superradiant states (with  $\tilde{\Gamma}_n > \Gamma_{\text{eff}}$ ) and a significant proportion of subradiant states (with  $\tilde{\Gamma}_n < \Gamma_{\text{eff}}$ ), exhibiting a wide range of linewidths, as illustrated in the lower panel of Fig. 5(b). While for  $V_0 = 8J$ , the situation is quite different. As shown in Fig. 5(c), the wave functions of the atomic chain are highly localized. In this case, the decay of each collective mode to the waveguide is primarily attributable to the most excited atom, which has an excitation probability close to one. Therefore, the width of each resonance dip in the reflection spectrum [see the upper panel of Fig. 5(d)] and the width of each collective excitation amplitude [see the lower panel of Fig. 5(d)] are approximately equal to the effective decay rate  $\Gamma_{\text{eff}}$  of a single atom. Namely, all collective states exhibit nei-

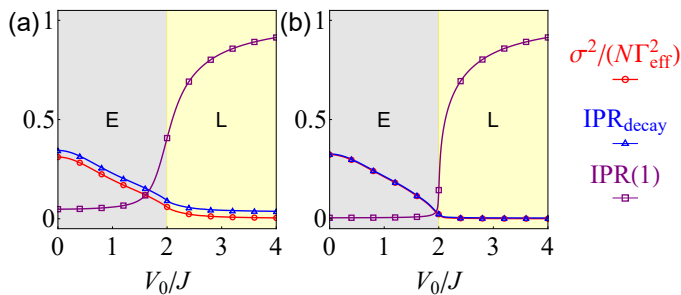


FIG. 6.  $\sigma^2$  and  $\text{IPR}_{\text{decay}}$  as functions of  $V_0$ , with (a)  $N = 30$ ,  $\delta = 0.1\gamma$ , and (b)  $N = 300$ ,  $\delta = 0.01\gamma$ . Other parameters are the same as those used in Fig. 5. The extended (E) and the localized (L) phases are well characterized by these quantities. In panels (a) and (b), the inverse participation ratio  $\text{IPR}(1)$  (Here 1 is used to denote the ground state) of the standard AAH chain is also provided for comparison.

ther a markedly superradiant nor a distinctly subradiant character.

A more straightforward illustration of the decay rates of the collective modes as a function of index  $n$  in the extended and localized phases can be found in Figs. 5(e) and 5(f), respectively. It can be observed that there exists an interesting correspondence between the extended (localized) phase of the atom array and the “localization” (“delocalization”) of the decay rates of its collective modes. We now seek ways to quantitatively characterize this correspondence. Note that the degree of localization of the  $n$ th eigenstate of the AAH chain can be described by the inverse participation ratio (IPR):

$$\text{IPR}(n) = \sum_m \left| \psi_m^{(n)} \right|^4, \quad (16)$$

which vanishes for extended states [see the curves marked with squares in Figs. 6(a) and 6(b)]. As for the aspect of the collective modes, the mean value of their decay rates is equal to the decay rate of a single atom, with  $(\sum_n \tilde{\Gamma}_n)/N = \Gamma_{\text{eff}}$ . It is therefore reasonable to conclude that the variance

$$\sigma^2 = \frac{1}{N} \sum_n \left( \tilde{\Gamma}_n - \Gamma_{\text{eff}} \right)^2 \quad (17)$$

may be employed as a means of measuring the concentration of the dissipation-rate distribution (vs index  $n$ ). It is evident that the variance  $\sigma^2 \simeq 0$  when  $V_0 > 2J$ , and  $\sigma^2 > 0$  when  $V_0 < 2J$  [see the curves marked with circles in Fig. 6(a) and 6(b)], indicating the localized and extended phases, respectively. Note that when  $V_0 \rightarrow 0$ , the order of magnitude of  $\sigma^2$  is  $N\Gamma_{\text{eff}}^2$  for an array with  $N \gg 1$ . This is due to the fact that in this regime, the decay rates of the superradiant modes, which are a few in number and of the order of  $N\Gamma_{\text{eff}}$ , contribute mainly to the variance. One can further define a “normalized” decay rate  $\tilde{\Gamma}'_n = \tilde{\Gamma}_n/(N\Gamma_{\text{eff}})$ , with  $\sum_n \tilde{\Gamma}'_n = 1$  (which is analogous to the normalization condition  $\sum_m |\psi_m^{(n)}|^2 = 1$

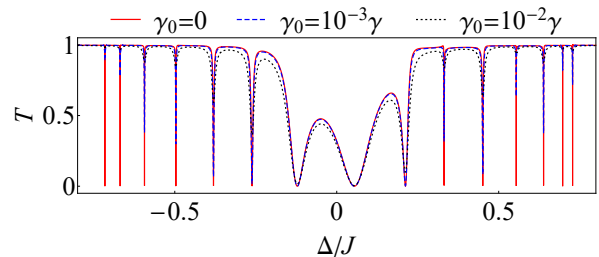


FIG. 7. Transmission coefficients as functions for different values of  $\gamma_0$ . The modulation frequency and the modulation phase are chosen as  $\beta = 1/4$  and  $\varphi = 0$ . Other parameters are the same as those used in Fig. 2(a). The range of  $\Delta$  is selected to display the spectrum corresponding to the center band.

of the wave functions). Therefore, it is possible to emulate the IPR for the wave functions [see Eq. (16)] to define the following IPR describing the distribution of the decay rates

$$\text{IPR}_{\text{decay}} = \sum_n \tilde{\Gamma}_n'^2. \quad (18)$$

The inverse of this quantity indicates the number of the collective modes that can decay appreciably into the waveguide. As shown in Fig. 6, both  $\sigma^2$  and  $\text{IPR}_{\text{decay}}$  can be used to quantify the localization transition. Moreover, in the thermodynamic limit  $N \rightarrow \infty$ , we have  $\sigma^2 = N\Gamma_{\text{eff}}^2 \times \text{IPR}_{\text{decay}}$ . This is consistent with the results (see the curves marked with circles and triangles) in Fig. 6(b), where a relatively large value of  $N = 300$  is chosen. Besides, a comparison of Figs. 6(a) and 6(b) illustrates that a finite-size system comprising a greater number of sites is more effective at exhibiting characteristics associated with quantum phase transitions.

In summary, the many-body state of the atomic chain is profoundly imprinted on the information contained within the single-photon scattering spectrum, making the localization transition easy to detect in wQED systems.

### E. Influence of spontaneous emission to channels other than the waveguide continuum

In practice, the unavoidable photon loss resulting from the coupling of the system with the surrounding environmental degrees of freedom should be taken into account. Assuming that all atoms have the same photon loss rate  $\gamma_0$ , the Hamiltonian (1) of the system can be rewritten as the following non-Hermitian one  $\hat{H}' = \hat{H} - (i\gamma_0/2) \sum_{i=1}^N \hat{\sigma}_i^+ \hat{\sigma}_i^-$ . The corresponding scattering amplitudes can be obtained by replacing the term  $\mathbf{H}$  in Eqs. (6a) and (6b) by  $\mathbf{H} - i\gamma_0\mathbf{I}/2$ . And the effective decay of the  $n$ th collective mode becomes  $\tilde{\Gamma}_n + \gamma_0$ . Obviously, the collective modes with small coupling rates to the waveguide (with  $\tilde{\Gamma}_n \ll \gamma_0$ ) are hardly excited due to



their extremely low coupling efficiency to the waveguide. Thus it can be observed from the transmission spectrum that the dips with narrower widths (corresponding to the subradiant states) are more significantly suppressed when a photon-loss rate  $\gamma_0$  is included, as shown in Fig. 7. For an atom array with dissipation rate of  $\gamma_0 = 10^{-3}\gamma$  (which can be achieved in current wQED setups based on superconducting quantum circuits [68]), all the collective modes of the atom array can still be probed by the transmission spectrum, including the extremely subradiant ones near the band edges, as shown by the blue dashed line in Fig. 7.

#### IV. CONCLUSION

In summary, we present an experimentally feasible scheme to simulate and probe the AAH model by utilizing giant-atom wQED systems. In our proposal, the coupling between a pair of neighboring atoms is generated by the nearly decoherence-free interaction mediated by the waveguide modes, thus eliminating the need for direct couplings between atoms. In addition to mediating interactions between atoms, the photonic modes in the waveguide are also used to detect the energy spectra of the atom array. Moreover, our method allows the energy spectrum of the atomic chain to be revealed by a single scattering process. As a result, the proposed system is characterized by a simple structure and high detection efficiency. In addition, the optimized parameters for achieving high-precision quantum simulation are analyzed to demonstrate the feasibility of the scheme under existing experimental techniques.

As specific examples, we first demonstrate the feasibility of precisely reconstructing the complex and fine fractal structure of the Hofstadter butterfly by utilizing the transmission spectrum. Subsequently, we show that in the case of incommensurate diagonal AAH model, the statistical distribution of the linewidths of the collective modes can be employed as a means of quantifying the localization transition, thereby facilitating the detection of this transition.

Our method is also applicable to the construction and detection of other types of 1D atomic chains, thus paving the way for quantum simulations of more complex many-body states based on giant-atom wQED. Furthermore, the results of this study suggest that wQED with giant atoms is an ideal platform for investigating light-matter interactions between a coupled qubit (or spin) chain and its photonic environment.

#### ACKNOWLEDGMENTS

This work was supported by the National Natural Science Foundation of China (NSFC) under Grants No. 61871333.

#### Appendix A: Scattering amplitudes expressed in terms of collective modes

To better understand the physics of the scattering process, we rewrite the scattering amplitudes (6a) and (6b) in terms of collective modes of the atom array:

$$t = 1 - i \sum_{n=1}^N \frac{(\mathbf{V}^\dagger \mathbf{U}_n^{\mathcal{R}})(\mathbf{U}_n^{\mathcal{L}\dagger} \mathbf{V})}{\Delta - \lambda_n}, \quad (\text{A1a})$$

$$r = -i \sum_{n=1}^N \frac{(\mathbf{V}^\top \mathbf{U}_n^{\mathcal{R}})(\mathbf{U}_n^{\mathcal{L}\dagger} \mathbf{V})}{\Delta - \lambda_n}, \quad (\text{A1b})$$

where  $\mathbf{U}_n^{\mathcal{R}}$  and  $\mathbf{U}_n^{\mathcal{L}}$  are the right and left eigenvectors of the non-Hermitian Hamilton matrix  $\mathbf{H}$ , and  $\lambda_n$  is the corresponding complex eigenvalues, satisfying  $\mathbf{H}\mathbf{U}_n^{\mathcal{R}} = \lambda_n \mathbf{U}_n^{\mathcal{R}}$ ,  $\mathbf{H}^\dagger \mathbf{U}_n^{\mathcal{L}} = \lambda_n^* \mathbf{U}_n^{\mathcal{L}}$ , and  $\mathbf{U}_n^{\mathcal{L}\dagger} \mathbf{U}_{n'}^{\mathcal{R}} = \mathbf{U}_n^{\mathcal{R}\dagger} \mathbf{U}_{n'}^{\mathcal{L}} = \delta_{nn'}$  [69]. The numerators in Eqs. (A1a) and (A1b) represent the overlap degree of the  $n$ th collective state of atomic chain and the propagating photon modes.

Equations (A1a) and (A1b) show that the scattering spectrum can be regarded as the result of interference between different scattering channels, which are provided by the corresponding collective modes. Under the Markovian approximation, the input  $\mathbf{V}$ , the Hamiltonian  $\mathbf{H}$ , and consequently the eigenvalues  $\lambda_n$  and eigenvectors  $\mathbf{U}_n^{\mathcal{R},\mathcal{L}}$  of  $\mathbf{H}$ , are independent of the frequency of the photons. Accordingly, the eigen frequency (with respect to the reference frequency  $\omega_a$ ) and the effective decay of the  $n$ th collective mode can be defined as  $\tilde{\Delta}_n = \text{Re}(\lambda_n)$  and  $\tilde{\Gamma}_n = -2\text{Im}(\lambda_n)$ , respectively. Further, we can define the weight factors  $\eta_n = -2i[(\mathbf{V}^\dagger \mathbf{U}_n^{\mathcal{R}})(\mathbf{U}_n^{\mathcal{L}\dagger} \mathbf{V})]/\tilde{\Gamma}_n$  and  $\xi_n = -2i[(\mathbf{V}^\top \mathbf{U}_n^{\mathcal{R}})(\mathbf{U}_n^{\mathcal{L}\dagger} \mathbf{V})]/\tilde{\Gamma}_n$ . Thus the transmission and reflection amplitudes can be written as

$$t = 1 + \sum_{n=1}^N \frac{\eta_n \tilde{\Gamma}_n}{2 \left( \Delta - \tilde{\Delta}_n + i \frac{\tilde{\Gamma}_n}{2} \right)}, \quad (\text{A2a})$$

$$r = \sum_{n=1}^N \frac{\xi_n \tilde{\Gamma}_n}{2 \left( \Delta - \tilde{\Delta}_n + i \frac{\tilde{\Gamma}_n}{2} \right)}. \quad (\text{A2b})$$

The above equations illustrate the superposition of several Lorentzian-type amplitudes contributed by the collective excitations, which is very helpful for us to analyze the scattering spectra for multi-atom wQED.

- 
- [1] D. Roy, C. M. Wilson, and O. Firstenberg, *Rev. Mod. Phys.* **89**, 021001 (2017).
- [2] X. Gu, A. F. Kockum, A. Miranowicz, Y.-x. Liu, and F. Nori, *Phys. Rep.* **718-719**, 1 (2017).
- [3] A. S. Sheremet, M. I. Petrov, I. V. Iorsh, A. V. Poshakinskiy, and A. N. Poddubny, *Rev. Mod. Phys.* **95**, 015002 (2023).
- [4] A. F. Kockum, in *International Symposium on Mathematics, Quantum Theory, and Cryptography*, Mathematics for Industry, edited by T. Takagi, M. Wakayama, K. Tanaka, N. Kunihiko, K. Kimoto, and Y. Ikematsu (Springer Singapore, Singapore, 2021) pp. 125–146.
- [5] G. Andersson, B. Suri, L. Guo, T. Aref, and P. Delsing, *Nat. Phys.* **15**, 1123 (2019).
- [6] B. Kannan, M. J. Ruckriegel, D. L. Campbell, A. F. Kockum, J. Braumüller, D. K. Kim, M. Kjaergaard, P. Krantz, A. Melville, B. M. Niedzielski, A. Vepsäläinen, R. Winik, J. L. Yoder, F. Nori, T. P. Orlando, S. Gustavsson, and W. D. Oliver, *Nature (London)* **583**, 775 (2020).
- [7] Z.-Q. Wang, Y.-P. Wang, J. Yao, R.-C. Shen, W.-J. Wu, J. Qian, J. Li, S.-Y. Zhu, and J. Q. You, *Nat. Commun.* **13**, 7580 (2022).
- [8] A. González-Tudela, C. S. Muñoz, and J. I. Cirac, *Phys. Rev. Lett.* **122**, 203603 (2019).
- [9] L. Du, Y. Zhang, J.-H. Wu, A. F. Kockum, and Y. Li, *Phys. Rev. Lett.* **128**, 223602 (2022).
- [10] H. Xiao, L. Wang, Z.-H. Li, X. Chen, and L. Yuan, *npj Quantum Inf.* **8**, 80 (2022).
- [11] A. F. Kockum, P. Delsing, and G. Johansson, *Phys. Rev. A* **90**, 013837 (2014).
- [12] L. Guo, A. Grimsmo, A. F. Kockum, M. Pletyukhov, and G. Johansson, *Phys. Rev. A* **95**, 053821 (2017).
- [13] L. Guo, A. F. Kockum, F. Marquardt, and G. Johansson, *Phys. Rev. Res.* **2**, 043014 (2020).
- [14] Q.-Y. Qiu, Y. Wu, and X.-Y. Lü, *Sci. China-Phys. Mech. Astron.* **66**, 224212 (2023).
- [15] K. H. Lim, W.-K. Mok, and L.-C. Kwek, *Phys. Rev. A* **107**, 023716 (2023).
- [16] L. Xu and L. Guo, *New J. Phys.* **26**, 013025 (2024).
- [17] Z. Y. Li and H. Z. Shen, *Phys. Rev. A* **109**, 023712 (2024).
- [18] F. Roccati and D. Cilluffo, *Phys. Rev. Lett.* **133**, 063603 (2024).
- [19] A. C. Santos and R. Bachelard, *Phys. Rev. Lett.* **130**, 053601 (2023).
- [20] X.-L. Yin and J.-Q. Liao, *Phys. Rev. A* **108**, 023728 (2023).
- [21] S. Guo, Y. Wang, T. Purdy, and J. Taylor, *Phys. Rev. A* **102**, 033706 (2020).
- [22] W. Zhao and Z. Wang, *Phys. Rev. A* **101**, 053855 (2020).
- [23] X. Wang, T. Liu, A. F. Kockum, H.-R. Li, and F. Nori, *Phys. Rev. Lett.* **126**, 043602 (2021).
- [24] W. Cheng, Z. Wang, and Y.-x. Liu, *Phys. Rev. A* **106**, 033522 (2022).
- [25] X. Zhang, C. Liu, Z. Gong, and Z. Wang, *Phys. Rev. A* **108**, 013704 (2023).
- [26] W. Z. Jia and M. T. Yu, *Opt. Express* **32**, 9495 (2024).
- [27] A. Ask, Y.-L. L. Fang, and A. F. Kockum, *arXiv:2011.15077*.
- [28] Q. Y. Cai and W. Z. Jia, *Phys. Rev. A* **104**, 033710 (2021).
- [29] S. L. Feng and W. Z. Jia, *Phys. Rev. A* **104**, 063712 (2021).
- [30] Y. T. Zhu, S. Xue, R. B. Wu, W. L. Li, Z. H. Peng, and M. Jiang, *Phys. Rev. A* **106**, 043710 (2022).
- [31] X.-L. Yin, Y.-H. Liu, J.-F. Huang, and J.-Q. Liao, *Phys. Rev. A* **106**, 013715 (2022).
- [32] Y. P. Peng and W. Z. Jia, *Phys. Rev. A* **108**, 043709 (2023).
- [33] W. Gu, H. Huang, Z. Yi, L. Chen, L. Sun, and H. Tan, *Phys. Rev. A* **108**, 053718 (2023).
- [34] W. Gu, L. Chen, Z. Yi, S. Liu, and G.-x. Li, *Phys. Rev. A* **109**, 023720 (2024).
- [35] A. F. Kockum, G. Johansson, and F. Nori, *Phys. Rev. Lett.* **120**, 140404 (2018).
- [36] A. Carollo, D. Cilluffo, and F. Ciccarello, *Phys. Rev. Res.* **2**, 043184 (2020).
- [37] L. Du, L. Guo, and Y. Li, *Phys. Rev. A* **107**, 023705 (2023).
- [38] A. Soro, C. S. Muñoz, and A. F. Kockum, *Phys. Rev. A* **107**, 013710 (2023).
- [39] R. P. Feynman, *Int. J. Theor. Phys.* **21**, 467 (1982).
- [40] I. M. Georgescu, S. Ashhab, and F. Nori, *Rev. Mod. Phys.* **86**, 153 (2014).
- [41] P. G. Harper, *Proc. Phys. Soc. Sect. A* **68**, 874 (1955).
- [42] S. Aubry and G. André, *Ann. Israel Phys. Soc* **3**, 133 (1980).
- [43] B. Simon, *Adv. Appl. Math.* **3**, 463 (1982).
- [44] D. J. Thouless, *Phys. Rev. B* **28**, 4272 (1983).
- [45] S. Ostlund, R. Pandit, D. Rand, H. J. Schellnhuber, and E. D. Siggia, *Phys. Rev. Lett.* **50**, 1873 (1983).
- [46] H. Hiramoto and M. Kohmoto, *Phys. Rev. Lett.* **62**, 2714 (1989).
- [47] S. Y. Jitomirskaya, *Ann. Math.* **150**, 1159 (1999).
- [48] S. Iyer, V. Oganessian, G. Refael, and D. A. Huse, *Phys. Rev. B* **87**, 134202 (2013).
- [49] S. Ganesan, K. Sun, and S. Das Sarma, *Phys. Rev. Lett.* **110**, 180403 (2013).
- [50] S. Lellouch and L. Sanchez-Palencia, *Phys. Rev. A* **90**, 061602 (2014).
- [51] F. Liu, S. Ghosh, and Y. D. Chong, *Phys. Rev. B* **91**, 014108 (2015).
- [52] V. Khemani, D. N. Sheng, and D. A. Huse, *Phys. Rev. Lett.* **119**, 075702 (2017).
- [53] D. R. Hofstadter, *Phys. Rev. B* **14**, 2239 (1976).
- [54] G. Roati, C. D’Errico, L. Fallani, M. Fattori, C. Fort, M. Zaccanti, G. Modugno, M. Modugno, and M. Inguscio, *Nature (London)* **453**, 895 (2008).
- [55] M. Schreiber, S. S. Hodgman, P. Bordia, H. P. Lüschen, M. H. Fischer, R. Vosk, E. Altman, U. Schneider, and I. Bloch, *Science* **349**, 842 (2015).
- [56] P. Bordia, H. Lüschen, U. Schneider, M. Knap, and I. Bloch, *Nat. Phys.* **13**, 460 (2017).
- [57] Y. Lahini, R. Pugatch, F. Pozzi, M. Sorel, R. Morandotti, N. Davidson, and Y. Silberberg, *Phys. Rev. Lett.* **103**, 013901 (2009).
- [58] Y. E. Kraus, Y. Lahini, Z. Ringel, M. Verbin, and O. Zeitlinger, *Phys. Rev. Lett.* **109**, 106402 (2012).
- [59] P. Roushan, C. Neill, J. Tangpanitanon, V. M. Bastidas, A. Megrant, R. Barends, Y. Chen, Z. Chen, B. Chiaro, A. Dunsworth, A. Fowler, B. Foxen, M. Giustina, E. Jef-

- frey, J. Kelly, E. Lucero, J. Mutus, M. Neeley, C. Quintana, D. Sank, A. Vainsencher, J. Wenner, T. White, H. Neven, D. G. Angelakis, and J. Martinis, *Science* **358**, 1175 (2017).
- [60] Y. Shi, Y. Liu, Y.-R. Zhang, Z. Xiang, K. Huang, T. Liu, Y. Wang, J. Zhang, C. Deng, G.-H. Liang, Z.-Y. Mei, H. Li, T. Li, W. Ma, H. Liu, C. Chen, T. Liu, Y. Tian, X. Song, S. P. Zhao, K. Xu, D. Zheng, F. Nori, and H. Fan, *Phys. Rev. Lett.* **131**, 080401 (2023).
- [61] H. Li, Y. Wang, Y. Shi, K. Huang, X. Song, G.-H. Liang, Z.-Y. Mei, B. Zhou, H. Zhang, J. Zhang, S. Chen, S. P. Zhao, Y. Tian, Z. Yang, Z. Xiang, K. Xu, D. Zheng, and H. Fan, *npj Quantum Inf.* **9**, 40 (2023).
- [62] H. Li, G.-H. Liang, Z.-Y. Mei, H. Yu, G. Xue, Y. Tian, X. Song, Z.-B. Liu, K. Xu, D. Zheng, F. Nori, and H. Fan, *Nat. Commun.* **14**, 5433 (2023).
- [63] J.-T. Shen and S. Fan, *Opt. Lett.* **30**, 2001 (2005).
- [64] J.-T. Shen and S. Fan, *Phys. Rev. Lett.* **95**, 213001 (2005).
- [65] C. R. Dean, L. Wang, P. Maher, C. Forsythe, F. Ghahari, Y. Gao, J. Katoch, M. Ishigami, P. Moon, M. Koshino, T. Taniguchi, K. Watanabe, K. L. Shepard, J. Hone, and P. Kim, *Nature (London)* **497**, 598 (2013).
- [66] L. A. Ponomarenko, R. V. Gorbachev, G. L. Yu, D. C. Elias, R. Jalil, A. A. Patel, A. Mishchenko, A. S. Mayorov, C. R. Woods, J. R. Wallbank, M. Mucha-Kruczynski, B. A. Piot, M. Potemski, I. V. Grigorieva, K. S. Novoselov, F. Guinea, V. I. Fal'ko, and A. K. Geim, *Nature (London)* **497**, 594 (2013).
- [67] B. Hunt, J. D. Sanchez-Yamagishi, A. F. Young, M. Yankowitz, B. J. LeRoy, K. Watanabe, T. Taniguchi, P. Moon, M. Koshino, P. Jarillo-Herrero, and R. C. Ashoori, *Science* **340**, 1427 (2013).
- [68] M. Mirhosseini, E. Kim, X. Zhang, A. Sipahigil, P. B. Dieterle, A. J. Keller, A. Asenjo-Garcia, D. E. Chang, and O. Painter, *Nature (London)* **569**, 692 (2019).
- [69] D. C. Brody, *J. Phys. A* **47**, 035305 (2013).